

Te-Doped Pd Nanocrystal for Electrochemical Urea Production by Efficiently Coupling Carbon Dioxide Reduction with Nitrite Reduction

Yonggang Feng,[†] Hao Yang,[†] Ying Zhang, Xiaoqing Huang,* Leigang Li, Tao Cheng, and Qi Shao*



Cite This: *Nano Lett.* 2020, 20, 8282–8289



Read Online

ACCESS |

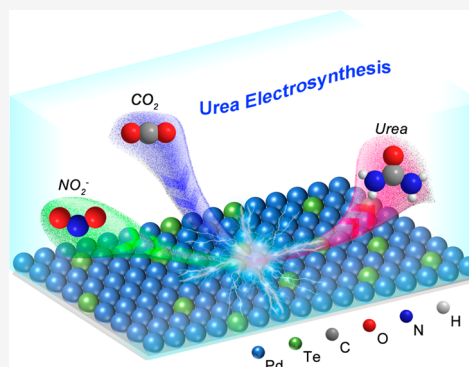
Metrics & More

Article Recommendations

Supporting Information

ABSTRACT: The renewable electricity-driven reduction of carbon dioxide (CO_2RR) is a promising technology for carbon utilization. However, it is still a challenge to broaden the application of CO_2RR . Herein, we report a Te-doped Pd nanocrystals (Te–Pd NCs) for promoting urea synthesis by coupling CO_2RR with electrochemical reduction of nitrite. The electrochemical synthesis of urea has been achieved with nearly 12.2% Faraday efficiency (FE) and 88.7% N atom efficiency (NE) at -1.1 V versus reversible hydrogen electrode (vs RHE), much higher than those of pure Pd NCs (4.2% FE and 21.8% NE). Significantly, an FE of $\sim 10.2\%$ and an NE of $\sim 82.3\%$ for urea solution production via an optimized flow cell system have been realized, where a solution with up to 0.95 wt % of urea has been obtained. Mechanistic insights show that Te-doping not only optimizes the CO_2/CO adsorption but also promotes NH_3 production, fully meeting the requirements of urea synthesis.

KEYWORDS: Coupling, Urea production, CO_2 electroreduction, Palladium, Tellurium



The renewable electricity-driven reduction of carbon dioxide (CO_2RR) represents a promising approach to generate sustainable fuels and chemicals that are currently manufactured using energy-intensive methods.^{1–4} It is already established that CO_2 can be exclusively converted into CO and formic acid,^{5–10} but the generation of further reduced products, especially multicarbon (C_{2+}) oxygenates and hydrocarbons (e.g., ethylene, ethanol) with higher energy densities, is more desirable in terms of economic efficiency and industrial applications.^{11–16} For the formation of C_{2+} products, the C–C coupling step is crucial yet highly sensitive to the catalyst, which is mainly achieved on Cu-based catalysts.^{13–17} Various nanostructured Cu catalysts have been explored to promote the formation of C_{2+} products, but it still suffers from high overpotential, poor C_{2+} selectivity, and serious hydrogen evolution reaction (HER).^{18,19} To this end, bonding C atoms of CO_2 with other available heteroatoms (e.g., N, S) in light of the formation mechanism for C_{2+} species is an alternative strategy to produce value-added products which is highly beneficial for expanding the application of CO_2RR .^{20–23}

Urea [$\text{CO}(\text{NH}_2)_2$], one of the most valuable industrial products, is an important nitrogen source for fertilizers and is produced worldwide at a scale of 100 million tons per year.^{24,25} In principle, the formation of C–N bonds of urea is possible along with CO_2RR when necessary nitrogen sources, such as nitrite ions (NO_2^-), and suitable catalysts are introduced.^{26–28} Nevertheless, the formidable challenge is that the parallel electroreduction of $\text{CO}_2/\text{NO}_2^-$ strongly competes with the

desired urea formation, resulting in complex products distribution, low Faradaic efficiency (FE) of urea as well as the difficulty of product separation. The simultaneous achievement of high FE and N atom efficiency (NE) of urea is highly desirable but remains challenging, which requires a catalyst with high CO selectivity for CO_2RR and privileged NH_3 production by NO_2RR . Pd-based nanomaterials have been widely recognized to possess high activity for CO_2RR and NO_2RR , but achieving high selectivity for a specific product is still challenging.^{29–32} Doping another metal into the Pd surface would be a feasible strategy, which can optimize the adsorption energy of the reaction species by tuning the surface electronic structure and further balance these competing electroreduction reactions to achieve the urea formation with both high FE and NE.

Motivated by the above discussion, we designed a Te-doped Pd nanocrystal (denoted as Te–Pd NC) with high CO FE (95.8%) for CO_2RR and high NH_3 NE (88.5%) for NO_2RR at -1.1 V versus reversible hydrogen electrode (vs RHE), outperforming those of the Pd NCs (54.2% CO FE for

Received: August 22, 2020

Revised: October 6, 2020

Published: October 14, 2020



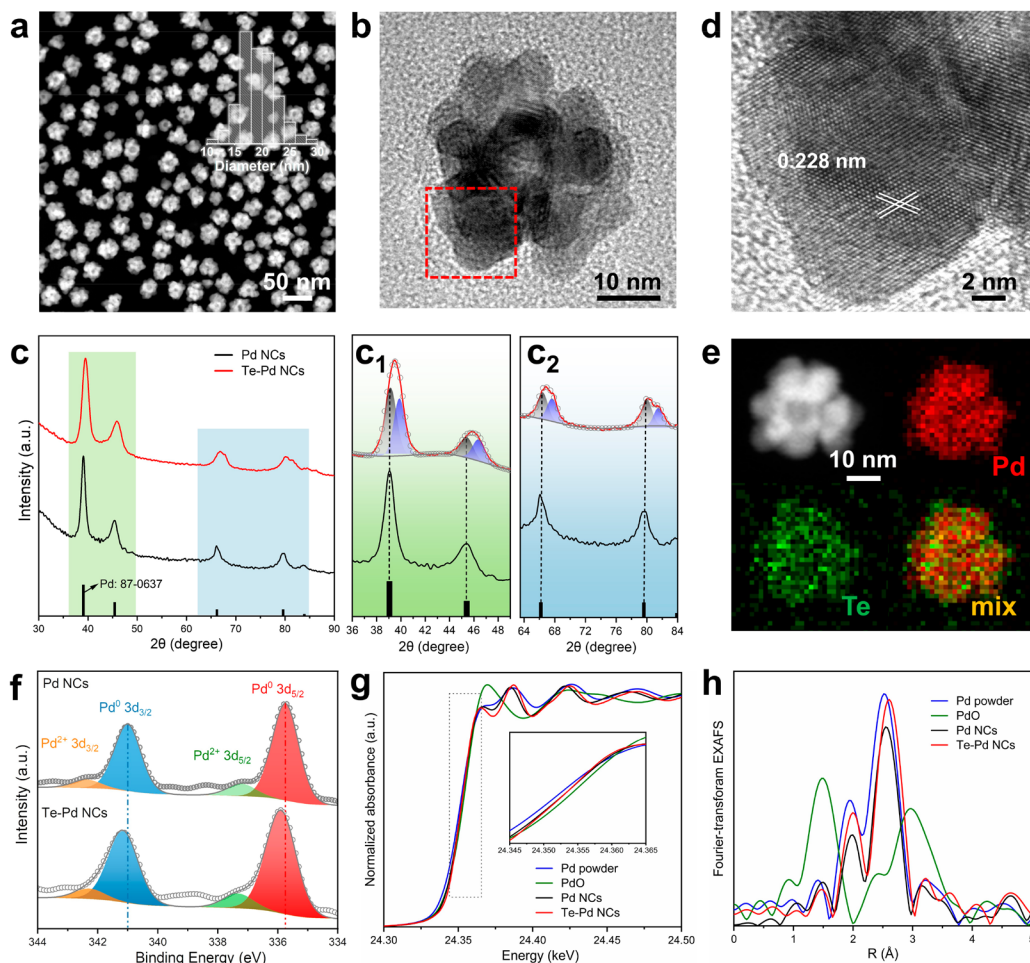


Figure 1. (a) HAADF-STEM image (up-right inset shows the corresponding diameter histogram) and (b) high-magnification TEM image of Te–Pd NCs. (c) PXRD patterns of Pd NCs and Te–Pd NCs. (c₁,c₂) Enlarged PXRD patterns from corresponding specific color area in (c). (d) HRTEM image of Te–Pd NCs from corresponding red rectangles in (b). (e) HAADF-STEM image and corresponding elemental mappings of Te–Pd NCs. (f) Pd 3d XPS spectra, (g) Pd K-edge XANES spectra and (h) Fourier-transform EXAFS of Te–Pd NCs and Pd NCs.

CO₂RR; 45.4% NH₃ NE for NO₂RR). By further simultaneously electroreducing CO₂ and NO₂⁻, electrochemical production of urea with nearly 12.2% FE and 88.7% NE was achieved at -1.1 V versus RHE, which is also much higher than those of the Pd NCs (4.2% FE; 21.8% NE). More significantly, an FE of ~10.2% and an NE of ~82.3% for urea solution production have been achieved by optimizing the measurement conditions of the flow cell system, where a urea concentration of up to 0.95 wt % has been obtained. The mechanistic insights into the urea electrosynthesis process show that Te-doping not only optimizes the CO₂/CO adsorption but also promotes NH₃ production, meeting the requirements of urea formation, which is expected to be achieved through the combination of *CO intermediates and NH₂-like intermediates on the catalyst.

The Te–Pd NCs were prepared by a wet-chemical approach, where Pd(acac)₂ and H₆TeO₆ are used as metal precursors and *N,N*-dimethylacetamide serves as solvent and reducing agent in tandem with NH₄HCO₃ and polyvinylpyrrolidone (PVP) (see Supporting Information for details). Similarly, Pd NCs were also prepared under the same conditions but in the absence of H₆TeO₆ (Figure S1). The high-angle annular dark-field scanning transmission electron microscopy (HAADF-STEM) image shows that the mono-dispersed Te–Pd NCs are uniform with an average diameter of

20 nm (Figure 1a). The high-magnification TEM images further reveal the discrete hierarchical nanostructure of Te–Pd NCs that is comprised of many subunits connected to the central core (Figure 1b). The powder X-ray diffraction (PXRD) pattern displays that all of the peaks of Pd NCs can be indexed to a face-centered cubic (*fcc*) unit cell, where the 2θ values of 39.1°, 45.4°, 66.2°, 79.6°, and 83.9° can be indexed to the diffraction of the (111), (200), (220), (311), and (222) planes of Pd (JCPDS card no. 87-0637). With Te doped, the PXRD peaks are obviously shifted to higher angles that are shown by the fitted peaks, indicating reduced *d*-spacing and the contraction of a lattice constant due to the doping of Te into the *fcc* Pd lattice (Figure 1c). The subtle difference of crystalline structure is further demonstrated by high-resolution TEM results. The lattice distance of Te–Pd NCs is approximately 0.228 nm, slightly smaller than that of Pd NCs (0.230 nm), which is assigned to the (111) plane of Pd (JCPDS card no. 87-0637) (Figure 1d and Figure S1c,d). The TEM energy-dispersive X-ray spectroscopy (TEM-EDS) result shows that the atomic ratio of Pd/Te in Te–Pd NCs is 91.4/8.6, consistent with the inductively coupled plasma-optical emission spectrometry (ICP-OES) result (89.2/10.8) (Figure S2). The HAADF-STEM image and corresponding elemental mappings demonstrate that the doped Te is distributed throughout the whole NC (Figure 1e). X-ray

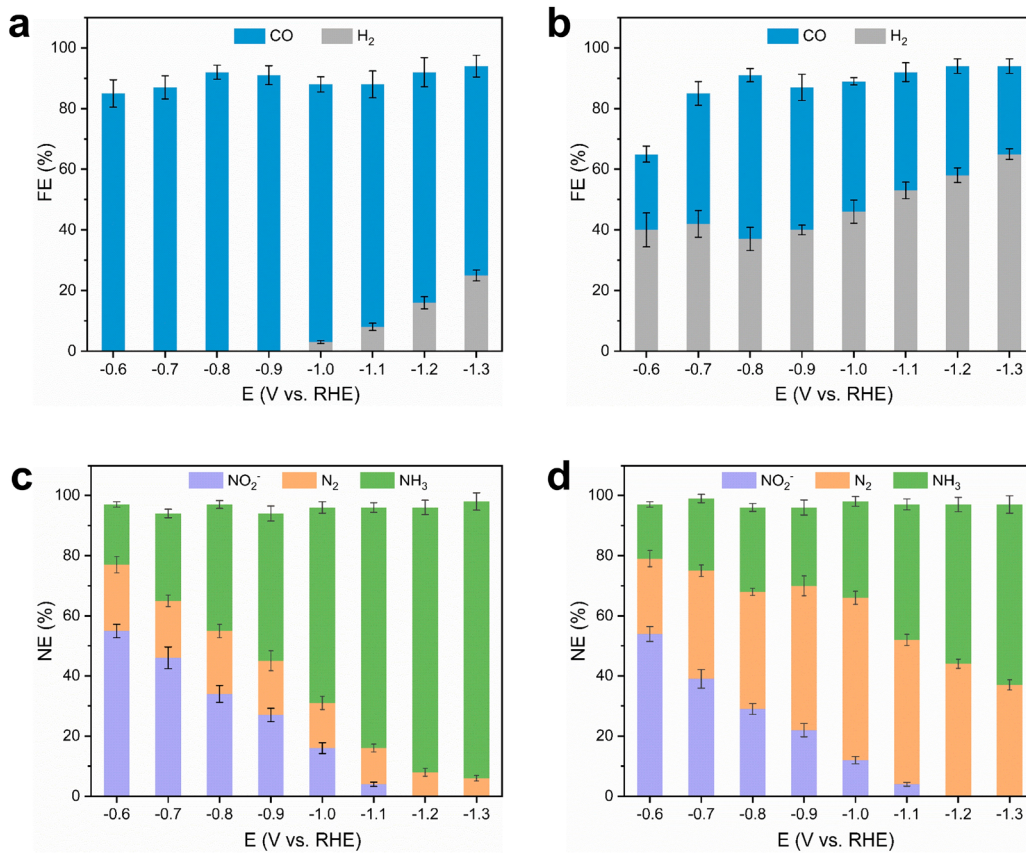


Figure 2. (a,b) CO and H₂ FE on (a) Te–Pd NCs/C and (b) Pd NCs/C for CO₂RR in CO₂-saturated 0.1 M KHCO₃ solution. (c,d) NO₂⁻, N₂ and NH₃ NE on (c) Te–Pd NCs/C and (d) Pd NCs/C for NO₂RR in 0.1 M KHCO₃ + 0.01 M KNO₃ solution.

photoelectron spectroscopy (XPS) was carried out to reveal the electronic interaction between Te and Pd. A couple of weak Te 3d peaks in Te–Pd NCs are observed (Figure S3). Meanwhile, the 3d_{3/2} and 3d_{5/2} peaks of Pd⁰ exhibit a small negative shift for Te–Pd NCs, suggesting slight electron transfer from Te to Pd (Figure 1f). The d-band of these NCs further confirms the electronic interaction between Pd and Te, where the center of gravity in Te–Pd NCs shifts down compared with that of Pd NCs (Figure S4). X-ray absorption near-edge structure (XANES) spectra are shown in Figure 1g, where the absorption edge of Te–Pd NCs is located at similar energy position to that of Pd powder, suggesting the Pd in Te–Pd NCs possesses metallic state. As for the lower intensity of Te–Pd NCs than that of Pd NCs, it is mainly attributed to the formation of Te-doped structure, which facilitates the transfer of electrons between Pd and Te, in agreement with the XPS results. Figure 1h shows the Pd extended X-ray absorption fine structure (EXAFS) R-space spectra, where the peaks observed at 1.9 and 2.6 Å for Te–Pd NCs and Pd NCs match with the Pd–Pd bond for Pd powder, indicating metallic Pd dominates in these catalysts.

The intrinsic CO₂RR and NO₂RR performance of catalysts was first investigated by using a H-cell system after loading Te–Pd NCs onto commercial carbon black (C, Vulcan XC-72R) (Figure S5). Figure S6a shows the linear sweep voltammograms (LSVs) recorded at 50 mV s⁻¹ for Te–Pd NCs/C casted on electrode in either Ar- or CO₂-saturated 0.1 M KHCO₃. Obvious current response is observed for Te–Pd NCs/C. Controlled potential electrolysis of CO₂ was then performed at different applied potentials between -0.6 and

-1.3 V versus RHE in CO₂-saturated 0.1 M KHCO₃ (Figure S6b). Under such conditions, only CO and H₂ were detected by online gas chromatography without other liquid products detected. Figure 2a shows FEs for the formation of CO and H₂ on Te–Pd NCs/C at different reduction potentials. Obviously, Te–Pd NCs/C presents much higher CO FE at various reduction potentials than Pd NCs/C (Figure 2b) with a maximum FE of 95.8% that is 1.8-fold higher than the maximum FE (54.2%) of Pd NCs/C at -0.8 V versus RHE, suggesting largely suppressed competitive HER on Te–Pd NCs/C. After establishing the baseline of CO₂ electrolysis activity, the performance of NO₂RR on the catalysts was then investigated. Figure S7a shows LSVs of NO₂RR on Te–Pd NCs, which presents a broad NO₂⁻ reduction peak between -0.6 and -0.9 V versus RHE. It is worth noting that the peak current on Pd NCs is higher than that on Te–Pd NCs, indicating relatively weak NO₂RR activity on Te–Pd NCs that may be due to the block of partial Pd active sites after Te doping. To precisely compare the activity of these catalysts for NO₂RR, the quantification of products formed during the prolonged electrolysis process was performed (see Supporting Information for details). The concentration of NO₂⁻ and generated NH₃ were determined by using the N-(1-naphthyl)-ethylenediamine dihydrochloride spectrophotometric method and the indophenol blue method, respectively (Figures S8 and S9). As shown in Figure 2c, the conversion of NO₂⁻ on Te–Pd NCs increases with the increased potential, but the product selectivity at different potentials displays large differences, where the main product is NH₃ at more negative potentials. A similar trend is also observed for Pd NCs (Figure 2d), but Te–

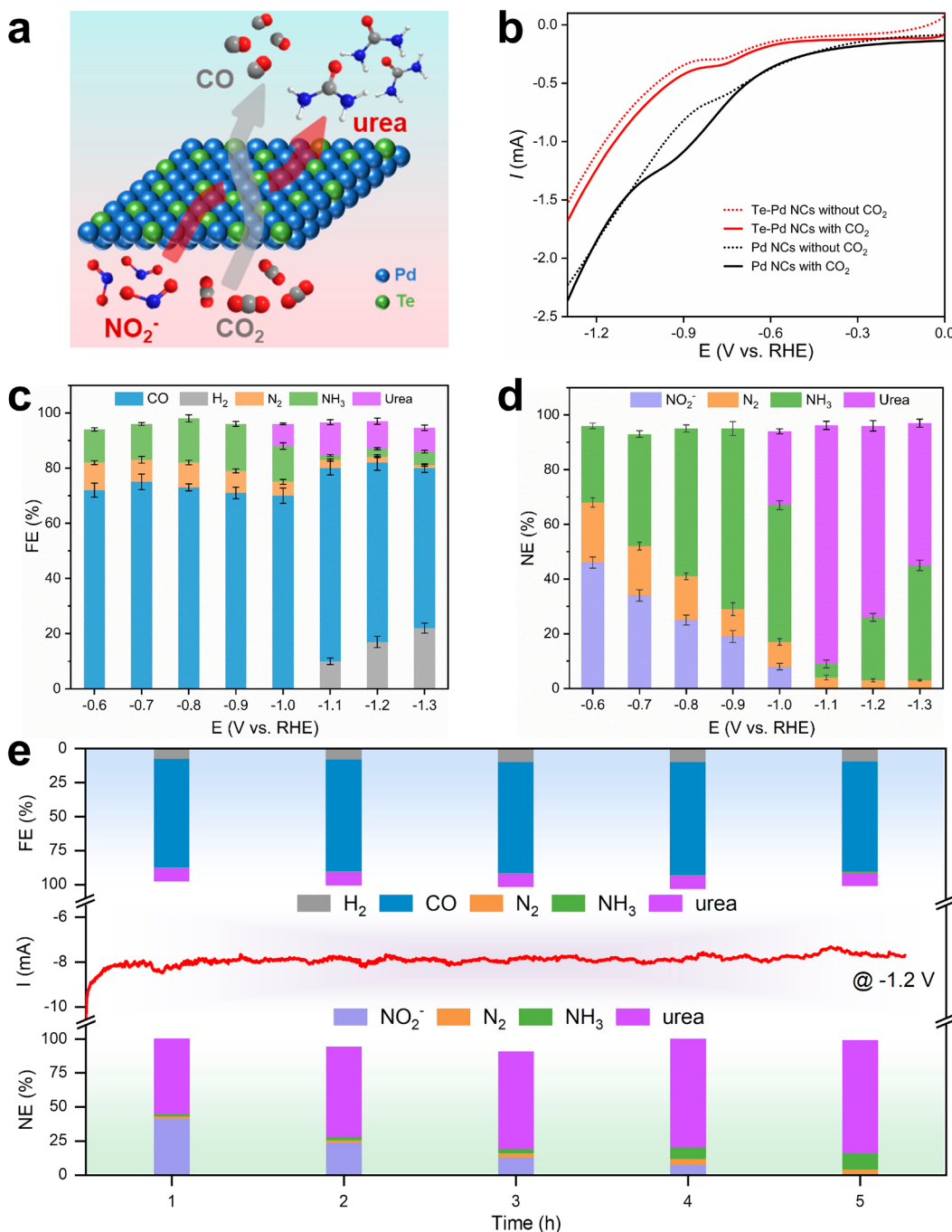


Figure 3. (a) A schematic depicts urea formation from simultaneous electroreduction of CO_2 and NO_2^- . (b) LSVs for electrolysis in $0.1 \text{ M KHCO}_3 + 0.01 \text{ M KNO}_2$ solution with and without CO_2 -saturated at a scan rate of 5 mV s^{-1} . (c) FE and (d) NE versus the applied potentials for urea electrosynthesis in CO_2 -saturated $0.1 \text{ M KHCO}_3 + 0.01 \text{ M KNO}_2$ solution on Te-Pd NCs/C. (e) Stability tests for continuous generation of pure urea solution in 0.05 M KNO_2 electrolyte on Te-Pd NCs/C.

Pd NCs require more negative potential to attain the same NO_2^- NE and favor NH_3 production.

Encouraged by the enhanced CO_2RR and NO_2RR performance, the Te-Pd NCs were further adopted as a catalyst for urea electrosynthesis by simultaneously reducing CO_2 and NO_2^- (Figure 3a). The produced urea was decomposed by urease into ammonia, which was measured by using a spectrophotometer (Figure S10). In the presence of CO_2 , obvious current responses resulting from electroreduction of NO_2^- and CO_2 are observed for both Te-Pd NCs/C and Pd NCs/C (Figure 3b). Remarkably, the coexistence of CO_2 and

NO_2^- led to considerable production of urea on Te-Pd NCs with an FE up to 12.2% at -1.1 V versus RHE (Figure 3c and Figure S11). Under such conditions, the CO FE is lower than that without NO_2^- at various potentials, which is probably ascribed to the consumption of CO for urea formation and competition in parallel with NO_2RR , whereas H_2 FE was maintained at high overpotentials. To precisely show N atom distribution during the urea formation process, the NE results were also acquired (Figure 3d). The conversion of NO_2^- and production of NH_3 in the presence of CO_2 are slightly increased at low potentials compared to that without CO_2 .

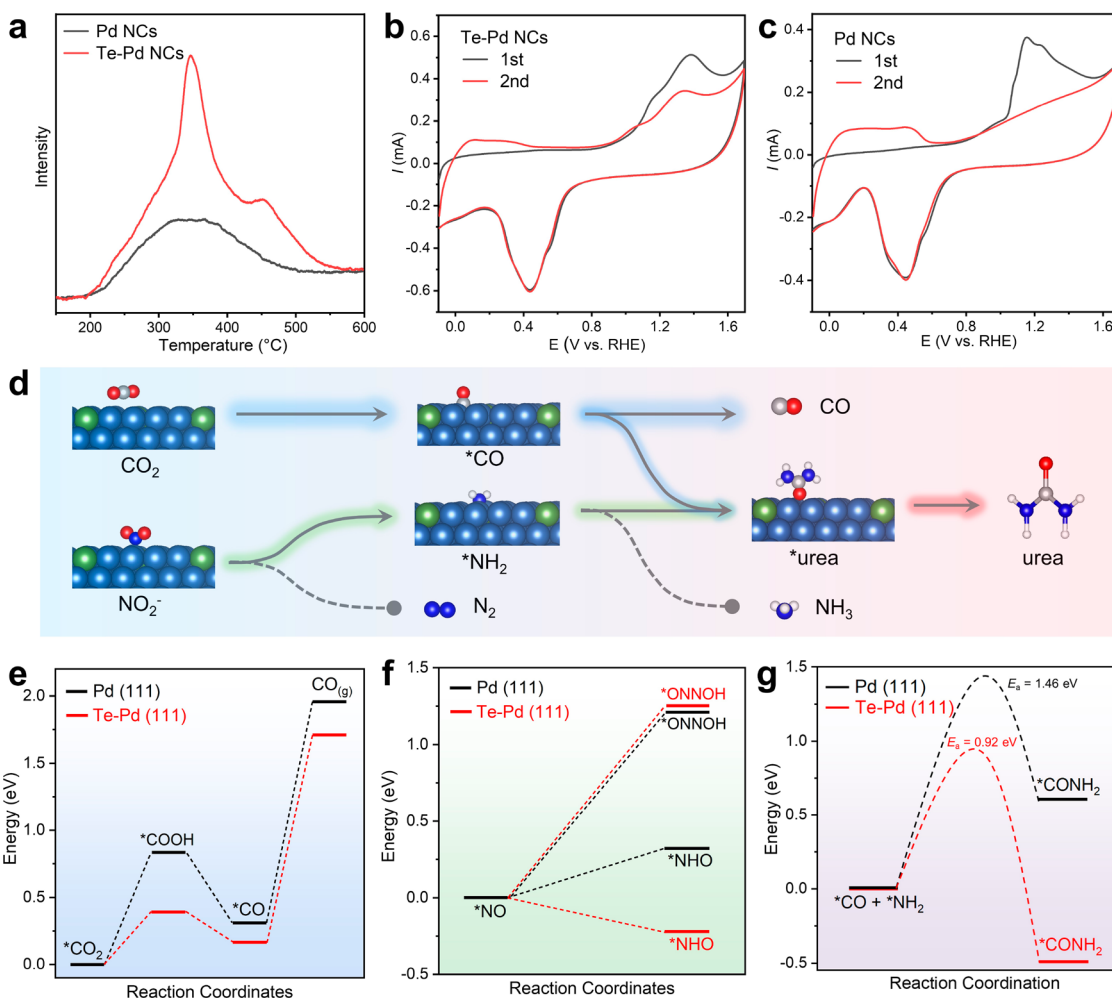


Figure 4. (a) CO₂-TPD profiles of Pd NCs and Te-Pd NCs. CO-stripping measurements of (b) Te-Pd NCs/C and (c) Pd NCs/C recorded in 0.1 M KHCO₃ solution at a scan rate of 20 mV s⁻¹ with (the first cycle) and without (the second cycle) a CO absorbed adlayer. CO was dosed for 30 min before each measurement. (d) Scheme of the urea synthesis from CO₂RR and NO₂⁻RR on Te-Pd NCs. Free energy profiles of (e) *CO₂ reduction to CO and (f) *NO reduction on pure Pd (111) and Te-doped Pd (111) surface, respectively. The “*” represents the active site. (g) Diagram of free energy changes and activation barriers of *CONH₂ formation on the Te-Pd (111) surface and pure Pd (111) surface, respectively.

Significantly, the maximum urea NE reaches 88.7% at -1.1 V versus RHE, indicating that the produced NH₃ from NO₂⁻RR is almost used for urea formation. On the contrary, Pd NCs/C exhibits very low urea FE (4.2% at -1.2 V versus RHE), mainly attributed to its low selectivity to CO and NH₃ (Figure S12a). The NE results for Pd NCs/C demonstrate that the maximum urea NE only accounts for 21.8% at -1.2 V versus RHE, but the formation of N₂ dominates in the conversion process (Figure S12b). In addition, the influence of NO₂⁻ concentration to urea formation was also investigated. Figure S13 shows the products FE and NE of the simultaneous reduction of CO₂ and various concentrations of NO₂⁻ over Te-Pd NCs/C at -1.1 V versus RHE. The NH₃ FE increases with increasing NO₂⁻ concentration and then becomes constant at concentrations higher than 0.05 M. In contrast, the CO FE and urea FE both decrease obviously with increasing NO₂⁻ concentration possibly due to the strong competition of the NH₃ formation during NO₂⁻RR (Figure S13a). By increasing the NO₂⁻ concentration, the NO₂⁻ NE greatly increases with enhanced NH₃ formation but reduced urea NE, indicating that lower NO₂⁻ concentration facilitates the formation of urea with high NE under these conditions (Figure S13b).

On the basis of the above impressive results of urea electroynthesis in the H-cell system, a flow cell system with a gas diffusion layer electrode was further used to obtain urea solution to overcome the inherent mass transport limitation. After optimizing the reaction conditions, the urea electroynthesis in the flow cell system was performed in 0.05 M KNO₃ at -1.2 V versus RHE (see Supporting Information for details). The CO formation also dominates in the CO₂RR process (~81.5% FE) with no liquid products from CO₂RR detected under such condition (Figure 3e). The urea FE (~10.2%) keeps constant in this process, while the urea NE increases with reaction time and reaches the maximum value (82.3%) after 5 h. A product solution with a urea concentration of up to 0.95 wt % was obtained. The detailed characterizations for the catalysts after long-time urea electrosynthesis were also carried out. It is clear to see that there are no obvious morphology/composition changes. PXRD result reveals that the peaks are still shifted to higher angles as freshly prepared Te-Pd NCs. Uniform elemental distributions have been further confirmed by the elemental mappings (Figure S14).

To unravel the possible mechanism, several control experiments were performed. First, CO₂-temperature-pro-

grammed desorption (TPD) was performed to study the CO₂ adsorption strength. As shown in Figure 4a, a peak corresponding to CO₂ desorption was observed at ~340 °C in the CO₂-TPD curve of Pd NCs. For Te–Pd NCs, the CO₂ desorption peak obviously shifts to higher temperature, giving two peaks at ~350 and 450 °C in the CO₂-TPD curve (Figure 4a). The positive shift of peak position and increase of peak area suggest that Te–Pd NCs exhibit much stronger CO₂ adsorption than Pd NCs. Moreover, the electrochemical CO-stripping measurement was carried out to study the stability of catalysts against CO poisoning.³³ It was found that a weak CO-stripping peak was observed on Te–Pd NCs/C around 1.3 V versus RHE (Figure 4b), while a much stronger CO-stripping peak was observed on Pd NCs/C, suggesting Te–Pd NCs/C exhibit higher stability against CO poisoning that mostly is due to the elimination of the part of strong absorption sites by doping with Te (Figure 4c). Furthermore, NH₃·H₂O and CO were used as feedstocks to elucidate the specific role of CO and NH₃ during electrocatalysis. As shown in Figure S1a, when 0.01 M NH₃·H₂O was added the FE for CO and H₂ were ~6% and ~85%, respectively. Further increase of the NH₃·H₂O concentration to 0.05 M results in a negligible influence on the FE of CO and H₂ (Figure S1b). Moreover, another contrast experiment was performed in CO-saturated 0.1 M KHCO₃ with different concentrations of KNO₂ on Te–Pd NCs/C. Only N₂ and NH₃ were observed in the products, even when the concentration of KNO₂ was increased from 0.01 to 0.05 M (Figure S16). The absence of urea in the above two control experiments indicates that CO₂ and NO₂[−] may be reduced into *CO and *NH₂, respectively, and further converted into urea on Te–Pd NCs/C, as illustrated in Figure 4d.

Density functional theory (DFT) calculations were performed to investigate the underlying mechanism. For DFT calculations, the Te–Pd NCs were simulated by constructing a 5 × 4 × 3 Pd(111) surface slab model with two Pd atoms replaced by one Te atom (Te–Pd(111)), leading to a Pd/Te ratio of 9:1 that is consistent with results from characterizations (see the Supporting Information for details). For CO₂ reduction to CO, it can be seen that both the formation of *COOH as well as the desorption of CO are downhill after the doping of Te in Pd(111), indicating that the obvious performance improvement of CO₂RR on Te–Pd (Figure 4e). On the other hand, the binding energy of CO on the Te–Pd(111) surface decreases by 0.25 eV in comparison to that on the Pd(111) surface, indicating that Te doping can significantly boost the CO₂RR performance. For NO₂RR, one needs to suppress the N₂ evolution, since the formation of *NH₂ and N₂ completely occurs during NO₂RR.³⁴ As depicted in Figure 4f, DFT calculations suggest *NO hydrogenation (*NHO) preferentially occurs on the Te–Pd(111) surface. In particular, the formation energy of *NHO intermediate is −0.22 eV, which is obviously lower than that of *ONNOH (1.25 eV), indicating that N₂ formation via N–N coupling is strongly suppressed on the Te–Pd(111) surface. For the Pd(111) surface, the energy difference between *NHO and *ONNOH is much smaller than that of the Te–Pd(111) surface, suggesting that N₂ formation may competitively occur on Pd NCs. In addition, the energy barrier for *CONH₂ formation from *CO with *NH₂ was further calculated, as shown in Figure 4g. It is found that the formation energy of *CONH₂ on Te–Pd(111) is −0.49 eV, which is much lower than that of pure Pd (0.61 eV). On the other hand, the energy

barriers of *CONH₂ on Te–Pd(111) surface and Pd(111) surface are 0.92 and 1.46 eV, respectively, indicating that urea formation is thermodynamically and kinetically preferred on the Te–Pd(111) surface, which is in good agreement with our experimental observations.

In summary, we demonstrate a promising strategy for the electrochemical synthesis of urea by integrating CO₂RR and NO₂RR on Te–Pd NCs/C. Results show the FE and NE of urea reach 12.2% and 88.7% at −1.1 V versus RHE on Te–Pd NCs/C. More importantly, by optimizing the measurement conditions in the flow cell system, the concentration of urea reaches 0.95 wt % with a urea FE and NE of ~10.2% and ~82.3%, respectively. Mechanism studies and theoretical calculations suggest that the synergy between Te and Pd in Te–Pd NCs significantly promotes CO₂RR to *CO, NO₂RR to *NH₂, and the reaction between *CO and *NH₂ for urea formation. More importantly, N₂ formation via NO₂RR, which competitively occurs on Pd NCs, is strongly suppressed on Te–Pd NCs. Consequently, Te–Pd NCs exhibit a much higher FE and NE for urea in comparison to pure Pd NCs. This work may not only provide an alternative strategy for urea synthesis to the conventional energy-consuming process but also promote the research in CO₂RR for high value-added chemicals.

ASSOCIATED CONTENT

Supporting Information

The Supporting Information is available free of charge at <https://pubs.acs.org/doi/10.1021/acs.nanolett.0c03400>.

Experimental details and data; Figures S1–S16 (PDF)

AUTHOR INFORMATION

Corresponding Authors

Xiaoqing Huang – State Key Laboratory of Physical Chemistry of Solid Surfaces, College of Chemistry and Chemical Engineering, Xiamen University, Xiamen 361005, China; College of Chemistry, Chemical Engineering and Materials Science, Soochow University, Jiangsu 215123, China; Email: hxq006@xmu.edu.cn

Qi Shao – College of Chemistry, Chemical Engineering and Materials Science, Soochow University, Jiangsu 215123, China; Guangdong Provincial Key Laboratory of Energy Materials for Electric Power, Southern University of Science and Technology, Shenzhen 518055, China;  orcid.org/0000-0002-9858-0458; Email: qshao@suda.edu.cn

Authors

Yonggang Feng – State Key Laboratory of Physical Chemistry of Solid Surfaces, College of Chemistry and Chemical Engineering, Xiamen University, Xiamen 361005, China; College of Chemistry, Chemical Engineering and Materials Science, Soochow University, Jiangsu 215123, China

Hao Yang – Institute of Functional Nano&Soft Materials (FUNSOM), Jiangsu Key Laboratory for Carbon-Based Functional Materials and Devices, Soochow University, Jiangsu 215123, China;  orcid.org/0000-0002-8241-6231

Ying Zhang – State Key Laboratory of Physical Chemistry of Solid Surfaces, College of Chemistry and Chemical Engineering, Xiamen University, Xiamen 361005, China

Leigang Li – College of Chemistry, Chemical Engineering and Materials Science, Soochow University, Jiangsu 215123, China

Tao Cheng – Institute of Functional Nano&Soft Materials (FUNSOM), Jiangsu Key Laboratory for Carbon-Based Functional Materials and Devices, Soochow University, Jiangsu 215123, China;  orcid.org/0000-0003-4830-177X

Complete contact information is available at:
<https://pubs.acs.org/10.1021/acs.nanolett.0c03400>

Author Contributions

[†]Y.F. and H.Y. contributed equally.

Author Contributions

X.H. and Q.S. conceived and supervised the research. X.H., Q.S., and Y.F. designed the experiments. X.H., Y.F., Y.Z., L.L., and Q.S. performed most of the experiments and data analysis. H.Y. and T.C. performed the section of DFT calculation. X.H., Q.S., Y.F., and Y.Z. participated in various aspects of the experiments and discussions. X.H., Q.S., and Y.F. wrote the paper. All authors discussed the results and commented on the manuscript.

Notes

The authors declare no competing financial interest.

ACKNOWLEDGMENTS

The authors thank the financial supports by the Ministry of Science and Technology of China (2016YFA0204100, 2017YFA0208200), the National Natural Science Foundation of China (2157113, 21905188, and 21975148), Young Thousand Talented Program, the Natural Science Foundation of Jiangsu Higher Education Institutions (17KJB150032 and SBK20190810), the project of scientific and technologic infrastructure of Suzhou (Szs201708), the Priority Academic Program Development of Jiangsu Higher Education Institutions (PAPD), China Postdoctoral Science Foundation Grant (2019M651937), Guangdong Provincial Key Laboratory of Energy Materials for Electric Power (No. 2018B030322001), and start-up support from Xiamen University. T.C. and H.Y. are supported by grants from startup supports of Soochow University and the Program for Jiangsu Specially-Appointed Professors to T.C.. H.Y. thanks China Postdoctoral Science Foundation (2019M660128) for financial support. We acknowledge Shanghai Supercomputer Center for providing the computational resources for this work. This work was partly supported by Collaborative Innovation Center of Suzhou Nano Science and Technology.

REFERENCES

- (1) Nielsen, D. U.; Hu, X. M.; Daasbjerg, K.; Skrydstrup, T. Chemically and electrochemically catalyzed conversion of CO₂ to CO with follow-up utilization to value-added chemicals. *Nat. Catal.* **2018**, *1*, 244–254.
- (2) De Luna, P.; Hahn, C.; Higgins, D.; Jaffer, S. A.; Jaramillo, T. F.; Sargent, E. H. What would it take for renewably powered electrosynthesis to displace petrochemical processes? *Science* **2019**, *364*, eaav3506.
- (3) Verma, S.; Lu, S.; Kenis, P. J. A. Co-electrolysis of CO₂ and glycerol as a pathway to carbon chemicals with improved technoeconomic due to low electricity consumption. *Nat. Energy* **2019**, *4*, 466–474.
- (4) Schiffer, Z. J.; Manthiram, K. Electrification and decarbonization of the chemical industry. *Joule* **2017**, *1*, 10–14.
- (5) Liu, S.; Tao, H.; Zeng, L.; Liu, Q.; Xu, Z.; Liu, Q.; Luo, J. Shape-Dependent electrocatalytic reduction of CO₂ to CO on triangular silver nanoplates. *J. Am. Chem. Soc.* **2017**, *139*, 2160–2163.

(6) Gu, J.; Hsu, C. S.; Bai, L.; Chen, H. M.; Hu, X. Atomically dispersed Fe³⁺ sites catalyze efficient CO₂ electroreduction to CO. *Science* **2019**, *364*, 1091–1094.

(7) Liu, S.; Lu, X. F.; Xiao, J.; Wang, X.; Lou, X. W. Bi₂O₃ nanosheets grown on multi-channel carbon matrix catalyze efficient CO₂ electroreduction to HCOOH. *Angew. Chem., Int. Ed.* **2019**, *58*, 13828–13833.

(8) Zhang, J.; Yin, R.; Shao, Q.; Zhu, T.; Huang, X. Amorphous InO_x nanoribbons for reinforced CO₂ electroreduction at broad potential by enhancing CO₂ adsorption and activation. *Angew. Chem., Int. Ed.* **2019**, *58*, 5609–5613.

(9) Sun, L.; Huang, Z.; Reddu, V.; Su, T.; Fisher, A. C.; Wang, X. A planar, conjugated N₄-macrocyclic cobalt complex for heterogeneous electrocatalytic CO₂ reduction with high activity. *Angew. Chem.* **2020**, *132*, 17252–17257.

(10) Wang, J.; Huang, X.; Xi, S.; Xu, H.; Wang, X. Axial modification of cobalt complexes on heterogeneous surface with enhanced electron transfer for carbon dioxide reduction. *Angew. Chem.* **2020**, *59*, 2–8.

(11) Weekes, D. M.; Salvatore, D. A.; Reyes, A.; Huang, A.; Berlinguet, C. P. Electrolytic CO₂ reduction in a flow cell. *Acc. Chem. Res.* **2018**, *51*, 910–918.

(12) Gao, D.; Arán-Ais, R. M.; Jeon, H. S.; Roldan Cuenya, B. Rational catalyst and electrolyte design for CO₂ electroreduction towards multi-carbon products. *Nat. Catal.* **2019**, *2*, 198–210.

(13) Dinh, C.-T.; Burdyny, T.; Kibria, M. G.; Seifitokaldani, A.; Gabardo, C. M.; Garcia de Arquer, F. P.; Kiani, A.; Edwards, J. P.; De Luna, P.; Bushuyev, O. S.; Zou, C.; Quintero-Bermudez, R.; Pang, Y.; Sinton, D.; Sargent, E. H. CO₂ electroreduction to ethylene via hydroxide-mediated copper catalysis at an abrupt interface. *Science* **2018**, *360*, 783–787.

(14) Zhuang, T. T.; Pang, Y.; Liang, Z.; Wang, Z.; Li, Y.; Tan, C.; Li, J.; Dinh, C. T.; De Luna, P.; Hsieh, P.; Burdyny, T.; Li, H.; Liu, M.; Wang, Y.; Li, F.; Proppe, A.; Johnston, A.; Nam, D.; Wu, Z.; Zheng, Y.; Ip, A. H.; Tan, H.; Chen, L.; Yu, S. H.; Kelley, S. O.; Sinton, D.; Sargent, E. H. Copper nanocavities confine intermediates for efficient electrosynthesis of C₃ alcohol fuels from carbon monoxide. *Nat. Catal.* **2018**, *1*, 946–951.

(15) Nitopi, S.; Bertheussen, E.; Scott, S. B.; Liu, X.; Engstfeld, A. K.; Horsch, S.; Seger, B.; Stephens, I. E. L.; Chan, K.; Hahn, C.; Nørskov, J. K.; Jaramillo, T. F.; Chorkendorff, I. Progress and perspectives of electrochemical CO₂ reduction on copper in aqueous electrolyte. *Chem. Rev.* **2019**, *119*, 7610–7672.

(16) Liang, Z. Q.; Zhuang, T. T.; Seifitokaldani, A.; Li, J.; Huang, C. W.; Tan, C. S.; Li, Y.; De Luna, P.; Dinh, C. T.; Hu, Y.; Xiao, Q.; Hsieh, P. L.; Wang, Y.; Li, F.; Quintero-Bermudez, R.; Zhou, Y.; Chen, P.; Pang, Y.; Lo, S. C.; Chen, L. J.; Tan, H.; Xu, Z.; Zhao, S.; Sinton, D.; Sargent, E. H. Copper-on-nitride enhances the stable electrosynthesis of multi-carbon products from CO₂. *Nat. Commun.* **2018**, *9*, 3828.

(17) Li, J.; Che, F.; Pang, Y.; Zou, C.; Howe, J. Y.; Burdyny, T.; Edwards, J. P.; Wang, Y.; Li, F.; Wang, Z.; De Luna, P.; Dinh, C. T.; Zhuang, T. T.; Saidaminov, M. I.; Cheng, S.; Wu, T.; Zou Finfrock, Y.; Ma, L.; Hsieh, S. H.; Liu, Y. S.; Botton, G. A.; Pong, W. F.; Du, X.; Guo, J.; Sham, T. K.; Sargent, E. H.; Sinton, D. Copper adparticle enabled selective electrosynthesis of n-propanol. *Nat. Commun.* **2018**, *9*, 4614.

(18) Vasileff, A.; Xu, C.; Jiao, Y.; Zheng, Y.; Qiao, S. Z. Surface and interface engineering in copper-based bimetallic materials for selective CO₂ electroreduction. *Chem.* **2018**, *4*, 1809–1831.

(19) Zhuang, T.; Nam, D.; Wang, Z.; Li, H.; Gabardo, C. M.; Li, Y.; Liang, Z.; Li, J.; Liu, X.; Chen, B.; Leow, W. R.; Wu, R.; Wang, X.; Li, F.; Lum, Y.; Wicks, J.; O'Brien, C. P.; Peng, T.; Ip, A. H.; Sham, T.; Yu, S. H.; Sinton, D.; Sargent, E. H. Dopant-tuned stabilization of intermediates promotes electrosynthesis of valuable C₃ products. *Nat. Commun.* **2019**, *10*, 1–7.

(20) Jouny, M.; Lv, J.-J.; Cheng, T.; Ko, B. H.; Zhu, J.-J.; Goddard, W. A.; Jiao, F. Formation of carbon-nitrogen bonds in carbon monoxide electrolysis. *Nat. Chem.* **2019**, *11*, 846–851.

- (21) Davies, B. J. V.; Saric, M.; Figueiredo, M. C.; Schjødt, N. C.; Dahl, S.; Moses, P. G.; Escudero-Escribano, M.; Arenz, M.; Rossmeisl, J. Electrochemically generated copper carbonyl for selective dimethyl carbonate synthesis. *ACS Catal.* **2019**, *9*, 859–866.
- (22) Garza, A. J.; Bell, A. T.; Head-Gordon, M. Mechanism of CO₂ reduction at copper surfaces: pathways to C₂ products. *ACS Catal.* **2018**, *8*, 1490–1499.
- (23) Chen, C.; Zhu, X.; Wen, X.; Zhou, Y.; Zhou, L.; Li, H.; Tao, L.; Li, Q.; Du, S.; Liu, T.; Yan, D.; Xie, C.; Zou, Y.; Wang, Y.; Chen, R.; Huo, J.; Li, Y.; Cheng, J.; Su, H.; Zhao, X.; Cheng, W.; Liu, Q.; Lin, H.; Luo, J.; Chen, J.; Dong, M.; Cheng, K.; Li, C.; Wang, S. Coupling N₂ and CO₂ in H₂O to synthesize urea under ambient conditions. *Nat. Chem.* **2020**, *12*, 717–724.
- (24) Qiao, J.; Liu, Y.; Hong, F.; Zhang, J. A review of catalysts for the electroreduction of carbon dioxide to produce low-carbon fuels. *Chem. Soc. Rev.* **2014**, *43*, 631–675.
- (25) Aresta, M.; Dibenedetto, A.; Angelini, A. Catalysis for the valorization of exhaust carbon: from CO₂ to chemicals, materials, and fuels. technological use of CO₂. *Chem. Rev.* **2014**, *114*, 1709–1742.
- (26) Shibata, M.; Yoshida, K.; Furuya, N. Electrochemical synthesis of urea at gas-diffusion electrodes IV. Simultaneous reduction of carbon dioxide and nitrate ions with various metal catalysts. *J. Electrochem. Soc.* **1998**, *145*, 2348–2353.
- (27) Shibata, M.; Yoshida, K.; Furuya, N. Electrochemical synthesis of urea at gas-diffusion electrodes Part II. Simultaneous reduction of carbon dioxide and nitrite ions at Cu, Ag and Au catalysts. *J. Electroanal. Chem.* **1998**, *442*, 67–72.
- (28) Shibata, M.; Furuya, N. Simultaneous reduction of carbon dioxide and nitrate ions at gas-diffusion electrodes with various metallophthalocyanine catalysts. *Electrochim. Acta* **2003**, *48*, 3953–3958.
- (29) Wang, J.; Kattel, S.; Hawxhurst, C. J.; Hoon Lee, J.; Tackett, B. M.; Chang, K.; Rui, N.; Liu, C.; Chen, J. G. Enhancing activity and reducing cost for electrochemical reduction of CO₂ by supporting palladium on metal carbides. *Angew. Chem., Int. Ed.* **2019**, *58*, 6271–6275.
- (30) Gao, D.; Zhou, H.; Cai, F.; Wang, J.; Wang, G.; Bao, X. Pd-Containing nanostructures for electrochemical CO₂ Reduction Reaction. *ACS Catal.* **2018**, *8*, 1510–1519.
- (31) Huang, H.; Jia, H.; Liu, Z.; Gao, P.; Zhao, J.; Luo, Z.; Yang, J.; Zeng, J. Understanding of strain effect in electrochemical reduction of CO₂; using Pd nanostructures as an ideal platform. *Angew. Chem., Int. Ed.* **2017**, *56*, 3594–3598.
- (32) Sun, C.; Li, F.; An, H.; Li, Z.; Bond, A. M.; Zhang, J. Facile electrochemical co-deposition of metal (Cu, Pd, Pt, Rh) nanoparticles on reduced graphene oxide for electrocatalytic reduction of nitrate/nitrite. *Electrochim. Acta* **2018**, *269*, 733–741.
- (33) Albers, P.; Pietsch, J.; Parker, S. F. Poisoning and deactivation of palladium catalysts. *J. Mol. Catal. A: Chem.* **2001**, *173*, 275–286.
- (34) Shin, H.; Jung, S.; Bae, S.; Lee, W.; Kim, H. Nitrite reduction mechanism on a Pd surface. *Environ. Sci. Technol.* **2014**, *48*, 12768–12774.